Background-free imaging of chemical bonds by a simple and robust frequency-modulated stimulated Raman scattering microscopy

HANQING XIONG,[1] NAIXIN QIAN,[1] ZHILUN ZHAO,[1] LINGYAN SHI,[1] YUPENG MIAO,[1] AND WEI MIN[1,2,*]

[1]*Department of Chemistry, Columbia University, New York, NY 10027, USA*
[2]*Kavli Institute for Brain Science, Columbia University, New York, NY 10032, USA*
[*]wm2256@columbia.edu

Abstract: Being able to image chemical bonds with high sensitivity and speed, stimulated Raman scattering (SRS) microscopy has made a major impact in biomedical optics. However, it is well known that the standard SRS microscopy suffers from various backgrounds, limiting the achievable contrast, quantification and sensitivity. While many frequency-modulation (FM) SRS schemes have been demonstrated to retrieve the sharp vibrational contrast, they often require customized laser systems and/or complicated laser pulse shaping or introduce additional noise, thereby hindering wide adoption. Herein we report a simple but robust strategy for FM-SRS microscopy based on a popular commercial laser system and regular optics. Harnessing self-phase modulation induced self-balanced spectral splitting of picosecond Stokes beam propagating in standard single-mode silica fibers, a high-performance FM-SRS system is constructed without introducing any additional signal noise. Our strategy enables adaptive spectral resolution for background-free SRS imaging of Raman modes with different linewidths. The generality of our method is demonstrated on a variety of Raman modes with effective suppressing of backgrounds including non-resonant cross phase modulation and electronic background from two-photon absorption or pump-probe process. As such, our method is promising to be adopted by the SRS microscopy community for background-free chemical imaging.

1. Introduction

Accelerating the spontaneous Raman scattering by many orders of magnitude, stimulated Raman scattering (SRS) microscopy has emerged as a powerful imaging modality of chemical bonds in biology, medicine and material science [1–6]. In the standard and most popular version of SRS microscopy, an intensity modulation (IM) is introduced to the Stokes (or pump) beam, and the vibrational resonance transfers this modulation to the loss (or gain) of the pump (or Stokes) beam, which generates a lock-in detectable stimulated-Raman signal [7,8]. Since the strong pump and Stokes laser pulses used in SRS imaging can also excite many competing processes, IM-based scheme unavoidably suffers from various backgrounds, which are unneglectable and can even be overwhelming in many cases [9–14]. Particularly, biological tissues are highly heterogeneous in refractive index, exhibiting non-resonant cross-phase modulation under laser excitation of high peak powers; chromophores (such as heme protein, melanin and exogenous dyes) are often encountered in SRS imaging, and their electronic resonance derived two-photon absorption or pump-probe background can be overwhelming. These backgrounds often limit the achievable contrast, quantification and sensitivity of the standard IM-based SRS microscopy.

Since most of the backgrounds exhibit much flatter spectral response than that of the target chemical bond, replacing the conventional IM by proper frequency modulation (FM) can effectively subtract the broadband backgrounds while maintaining the narrow-band signal. This principle is illustrated in Fig. 1 for the stimulated Raman Loss (SRL) case. The FM scheme

can be regarded as the combination of two IM excitations (one on-resonance and the other off-resonance) with a π phase difference, resulting in automatic cancelation of the broadband backgrounds while maintaining the narrowband signal under lock-in detection. Because of its effectiveness, FM has been intensively investigated from the very beginning of coherent Raman spectroscopy and microscopy. Starting from 1980s, several FM-SRS schemes have been reported by using home-build intracavity-modulated pulsed laser systems [15,16], synchronizing of several commercial picosecond-pulsed laser systems or amplifiers [17–19], precise shaping and controlling of broadband femtosecond pulses [10,13,20,21]. However, many of these FM methods require custom-built laser systems or non-trivial optical alignments, whose cost and technical complication have largely prevented them from being adopted in the wide SRS imaging community. Moreover, methods based on femtosecond pulse shaping, though effective in broadband label-free bio-imaging, have limited spectral resolution [10,13,20,21], especially for exciting those emerging vibrational probes with narrow Raman linewidth [11,22–24]. Furthermore, temporal fluctuations of the dual-frequency excitations in FM-SRS configuration can introduce additional noise for the signal contrast, which has not been well characterized in many previous demonstrations.
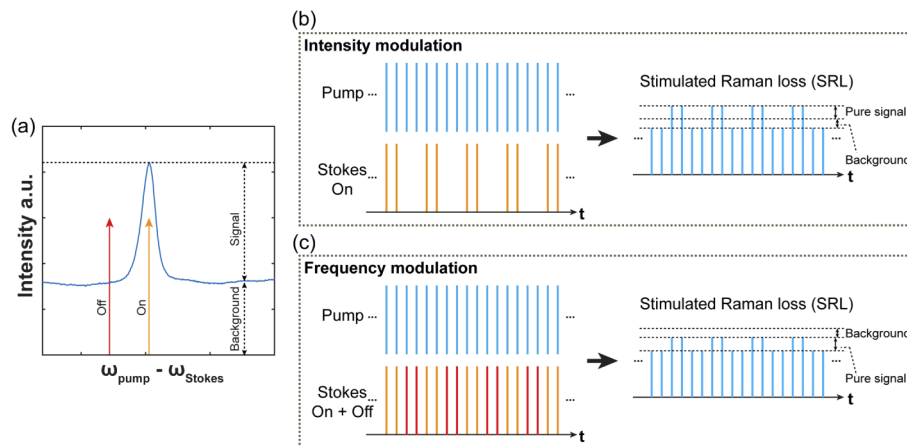

Fig. 1. The principle of intensity modulation (IM) and frequency modulation (FM) for stimulated Raman loss (SRL) detection. (a) shows a typical narrowband Raman peak on top of broadband backgrounds. Yellow line and red line show the on and the off resonance of stimulated Raman excitation, respectively. The backgrounds could originate from non-resonant four-wave mixing, electronic-transition-related backgrounds (such as two-photon absorption and hot luminescent, etc.), and even broadband Raman background from the environments. For IM case (b), only the intensity-modulated Stoke beam at vibrational-on-resonance wavelength is applied; for FM cases (c), two Stokes beams, one at the vibrational-on-resonance wavelength and the other one at the vibrational-off-resonance wavelength, intensity modulated with a π-phase difference, are applied. In (b) and (c), left columns show the input pulse sequences for both Stokes beams and pump beams, right columns show the pulse sequences of output Pump beams after interaction with the sample, respectively.

Here we report a simple but robust FM strategy based on self-phase modulation (SPM) of picosecond pulses propagating in standard single mode silica fibers. We note that, under proper nonlinear phase shift accumulated through SPM, the center frequency of the pulse will be nearly depleted, and the original peak will be replaced by new frequency lobes. Importantly, as a four-wave mixing process, the depleted photons in the center frequency are intrinsically equal-distributed to the two sidebands [25]. We thus harness this spectral splitting phenomenon for self-balanced dual-frequency SRS excitations to develop a new FM strategy without introducing

additional signal noise. Moreover, an adaptive spectral resolution can be chosen for Raman modes of different linewidths by simply controlling the laser power launched into the fiber. The effectiveness of our method is investigated on a variety of popular SRS imaging targets including label-free biomolecules, exogenous small molecule markers, and Raman dyes. Background-free SRS imaging is demonstrated by suppressing backgrounds of various spectroscopic origins including non-resonant cross-phase modulation and electronic-transition-derived backgrounds. As our method is built upon a popular commercial picosecond laser (currently installed in the integrated SRS microscope from Leica) and regular optics, it has a high potential to be readily adopted by the wide SRS microscopy community.

2. Results

2.1. Spectral splitting via self-phase modulation

Our method is inspired by one of the marvelous effects of ultrafast laser pulses propagating in optical fibers. As a laser pulse (such as a non-chirped sech^2 pulse) is propagating in a single-mode optical fiber, when the maximum nonlinear phase shift ϕ_{max} accumulated by SPM reaches 1.5π (with neglectable change on the pulse temporal profile), the center frequency of the pulse will be nearly depleted, and the original peak will be replaced by the spectral broadening of two new frequency lobes generated just near the center frequency (Fig. 2(a), (b)) [25,26]. The accumulated nonlinear phase is proportional to the field strength and propagation distance. A larger ϕ_{max} (due to a larger pulse power or a longer fiber) will result in a wider spectral broadening with multiple lobes and with the two margins having the maximum power denstity [25,27] (Fig. 2(a), (b)).

Numerical solution of the nonlinear Schrodinger equation (NSE) (details see Appendix A) can be used to illustrate the effect of spectral splitting above [28]. For the typical picosecond pulses used in SRS microscopy, a nJ-level pulse propagating in tens of cm of a standard single mode silica fiber will accumulate enough nonlinear phase shift to generate such frequency lobes. For example, our numerical results show that a 6.25-nJ 2-ps non-chirped sech^2 pulse with center wavelength at 1031.2-nm will generate two symmetric sidebands with ~1.4-nm wavelength difference (~13-cm^{-1}) after propagating in 0.2-m standard signal-mode silica fiber (6-μm mode field diameter) (Appendix A). For the fiber length within several meters (where SRS and group velocity dispersion can be omitted), the experiment configuration with the same products of pulse power and fiber length results in identical output spectra (Fig. 2(b), Appendix A). Importantly, by gradually increasing this product, the frequency difference between these lobes can be tuned from several cm^{-1} to tens of cm^{-1} (Fig. 2(b)), with little change introduced to the pulse temporal profile (Fig. 2(a)). This result suggests that adjusting the input pulse power and/or the fiber length could provide an easy way to control the output pulse spectrum.

Realizing that the energy separation (tens of cm^{-1}) of the two symmetric sidebands after SPM is comparable to the typical Raman linewidth, we proposed that this spectral splitting effect could serve as a mechanism to generate two close excitation frequencies for FM-SRS. Importantly, the four-wave mixing nature of SPM ensures the equal distribution of converted photons to the two sidebands (Fig. 2(c)). With such an intrinsic balance mechanism, a system with high stability and good noise properties can be expected. We then tested this idea in real pulses produced from a popular commercial laser system used for SRS imaging (PicoEmerald S, APE), which is non-Fourier-transform-limited and also full of ripples on the spectrum (Fig. 2(d)-(f), red dash). The pulses were directly launched into a polarization-maintained single-mode silica fiber (PM980-XP, Nufern) without dispersion correction. Interestingly, with a 6.2-nJ pulse energy (corresponding to 0.5-W with an 80-MHz repetition rate) propagating through a 0.2-m fiber, the 1-nm bandwidth of the 1031.2-nm infrared (IR) output is split to two sidebands near the center frequency. The measured separation between their energy centers is ~1.1-nm (~11-cm^{-1}) (Fig. 2(d)). Moreover, 0.6-nJ pulse propagating in 2-m results in similar output spectrum (Fig. 2(e)), as predicted by the theory for similar product of pulse energy and propagation
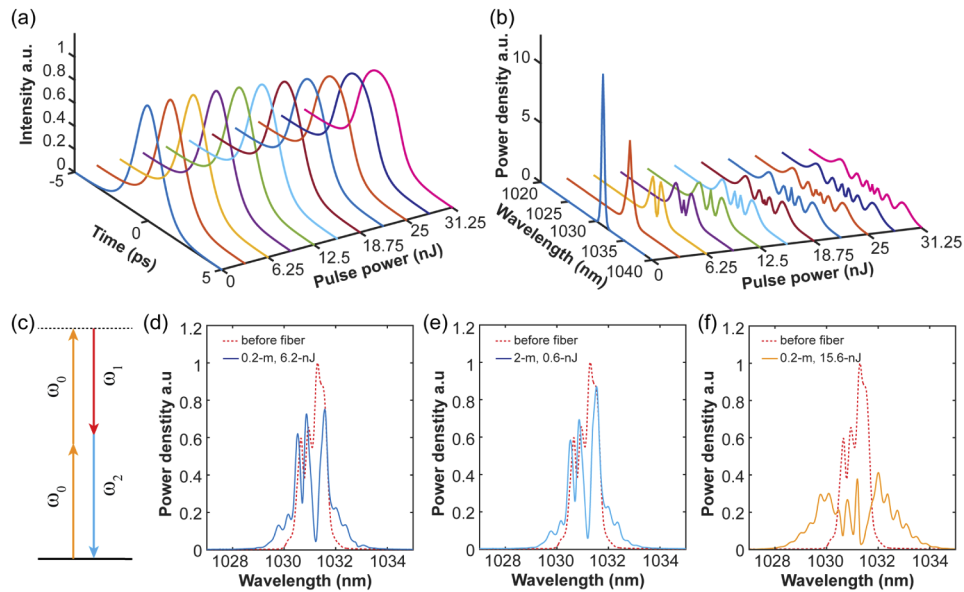
Fig. 2. Propagation and spectral splitting of picosecond laser pulses in single-mode silica fiber. (a) and (b) show the simulation results of temporal (a) and spectral (b) profiles of non-chirped 2-ps sech^2 pulses centered at 1031.2 nm after propagating in 0.2-m-long single-mode silica fiber as a function of the pulse power. All curves are normalized to the same pulse power. (c) The energy diagram of the self-phase modulation (SPM) process inside the fiber. (d) and (f) show the experiment results of 6.2-nJ (d) and 15.6-nJ (f) 2-ps pulses centered at 1031.2 nm after propagating through a 0.2-m polarization-maintained single-mode silica fiber. (e) shows the experiment result of 0.6-nJ 2-ps pulses centered at 1031.2 nm after propagating through a 2-m-long polarization-maintained single-mode silica fiber. For (d-f), red dash curves are spectra before fiber, solid curves are spectra output from the fiber, and all spectra are normalized to the same pulse power. The initial input pulse is not Fourier-transform-limited.

distance. Furthermore, coupling larger (15.6-nJ) pulse energy into the 0.2-m fiber increases the spectral separation to 27-cm^{-1}, accompanied by small energy sidebands (Fig. 2(f)). Hence, as supported by simulation and experiment, we can indeed split picosecond pulses to two closely lying excitation frequencies via SPM, and control their spectral separation by adjusting the power launched into the fiber or the length of the fiber.

2.2. Instrumentation of FM-SRS microscope

Figure 3(a) shows the design of our FM-SRS microscope with details in Appendix B. The standard commercial OPO system used here (PicoEmerald S, APE) is pumped by the second harmonic generation (SHG) of a 2-ps-pulsed IR laser centered at 1031.2 nm (80-MHz repetition rate), which enables optical-synchronized output of the IR beam and a tunable OPO signal beam. The tunable OPO signal (2-ps, 0.6-nm FWHM bandwidth) is used directly as the pump beam for SRS. After propagating through the 0.2-m long polarization-maintained single-mode silica fiber (PM980-XP, Nufern), the spectrally broadened IR beam is collimated and sent to a high efficiency grating (87% for S-polarization, T-1400-800, Lightsmyth), whose blaze direction is aligned parallel to the optical table. The spectrum of the beam is then projected onto a knife-edge mirror (MRAK25-E03, Thorlabs) through a doublet (f = 500 mm). The knife-edge mirror is

aligned near the focus plane of the doublet, which slices the spectrum to two symmetric bands, one blue shifted, and the other red shifted relative to the original IR beam, respectively.

After this, the two separated spectral bands propagate on two arms in the opposite direction. At the focus plane of each arm, the beam hits a mirror and reflects back. The mirror is slightly tilted in vertical direction, so that after repassing the grating, the two spectral bands can be picked out separately by mirrors at different heights. The grating is placed at the back-focus plane of the doublet. Hence spatial dispersion of the beams is cancelled after repassing the grating, and two collimated Stokes beams with different frequencies are generated. Note that the depletion of the center band will be symmetrically distributed into the newly generated two sidebands as a result of SPM (i.e. a four-wave mixing process). Thus, when the splitting edge of the knife-edge mirror is placed exactly on the dip of the SPM spectrum, the two Stokes arms are naturally balanced, and only slight adjustments of the waveplates on each arm is needed to compensate for the initial asymmetry. The polarizations of these two Stokes beams are then rotated to be perpendicular to each other, combined by a polarized beam splitter, and sent into an electro-optic modulator (EOM) (EO-PM-R-20-C1, Thorlabs). The orthogonal polarization introduces a π-phase shift between the modulation of the two beams, generating the standard FM Stokes beams (Fig. 1(c)). Finally, the Stokes beams after the EOM are combined with the pump beam (i.e., OPO signal) and coupled into a galvanometer-driven laser scanning microscope for SRS imaging. The time overlap between pump beam and two Stokes beams is controlled by two delay lines separately. And the whole alignment is sealed inside a box to avoid perturbations induced by the airflow.

2.3. Characterizations of FM-SRS microscope

Our FM-SRS design is based on relatively cheap and regular optical components, which is a big advantage compared with previous methods [10,13,15–20]. Comparing with the standard IM-SRS microscopy [7], the only hardware addition is on the Stokes beam line (red dash box in Fig. 3(a)). Figure 3(b) shows the correlation functions of each Stokes arm with the same pump beam, mapped by the SRL signal of broadband O-D stretching mode of liquid D_2O, respectively. The overlap indicates an equivalent ~2-ps pulse width for each Stokes arm, which is similar to the original IR pulse. As a result, no change to the SRS excitation efficiency has been observed compared to the original IR laser. It is important to note that, the frequency difference between the two Stokes arms of our design can be controlled by the pulse energy launched into the fiber and/or the length of the fiber independently (Fig. 2). This property enables an adaptive spectral resolution for Raman modes with varying linewidths, which will be systematically illustrated in the FM-SRS imaging applications presented later.

As mentioned above, the equal distribution of converted photons by SPM into the two spectral bands should ensure synchronized fluctuations of the two Stokes beams. This prediction was confirmed by our measurements (Fig. 3(c)-(h)): indeed, the fluctuations of the two Stokes beams exactly match each other (Fig. 3(c), (d)). To show this strong temporal correlation resulting in superb noise property of our FM-SRS microscope, we used the O-D stretching mode of liquid D_2O, whose broad Raman line shape is much wider than the energy separation of the two Stokes beams, to create a test signal distribution after scanning a field of view. Remarkably, the signal fluctuation excited by our FM-SRS displays the same distribution as that of the conventional IM-SRS under the same system configuration (Fig. 3(e)-(g)). Quantitatively, FM-SRS exhibits exactly the same noise model as that of the IM-SRS (Fig. 3(h)), indicating the good balance and spectral stability of the two Stokes beams. Otherwise, the excess noise term in the noise model (the coefficient of the quadratic term in the square root of Fig. 3(h)) would have to increase due to the stochastic transient unbalance.
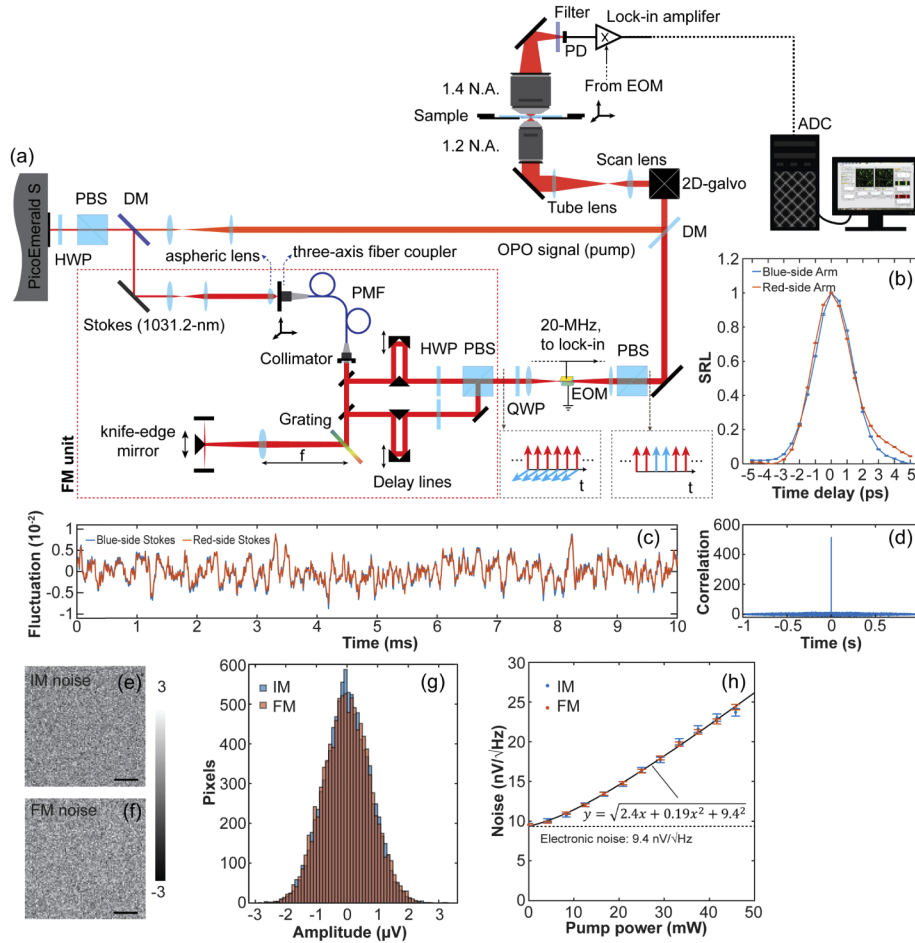
Fig. 3. Frequency-modulated (FM) stimulated Raman Scattering (SRS) microscopy achieved by self-phase modulation in silica fiber. (a) The systematic diagram. Gay dash boxes show the polarization of the Stokes pulses (red arrows for red-shifted Stokes beam, blue arrows for blue-shifted Stokes beam) at corresponding positions. (b) shows the SRL signal of O-D stretching mode of D_2O as a function of time delay between the pump beam and each Stokes beams. Blue curve for excitation energy blue-shifted arm (corresponding to red-shifted Stokes beam); red curve for excitation energy red-shifted arm (corresponding to blue-shifted Stokes beam). HWP for half-wave plate; PBS for polarized beam splitter; DM for dichroic mirror; PMF for polarization-maintained single mode fiber, the length used in this research is 0.2 m; QWP for quarter-wave plate; EOM for electrooptic modulator; OPO for optical parametric oscillator; PD for photodiode; ADC for analog-to-digital converter. (c) shows the real-time fluctuations of the two Stokes beams recoded by photodetectors with 1.9-MHz bandwidth. Red curve for red-side Stokes beam; blue curve for blue-side stokes beam. (d) shows the correlation of the fluctuations of two Stokes beams in 1-s time window. (e) and (f) shows the fluctuations of SRL signals of the broadband O-D stretching mode of D_2O excited by the conventional IM-SRS (e) and our FM-SRS (f) under the same configuration (46-mW pump beam at 820 nm, 15-mW stokes beams, and 1-kHz noise equivalent power (NEP) bandwidth). (g) shows the histograms of (e) and (f), respectively. (h) The noise as a function of the pump power for the conventional IM-SRS (blue dots) and our FM-SRS (red dots) under the same configuration (15-mW stokes beams, 1-kHz NEP bandwidth). Dots are measurements and the curve are fitting result. Scale bar: 10 μm.
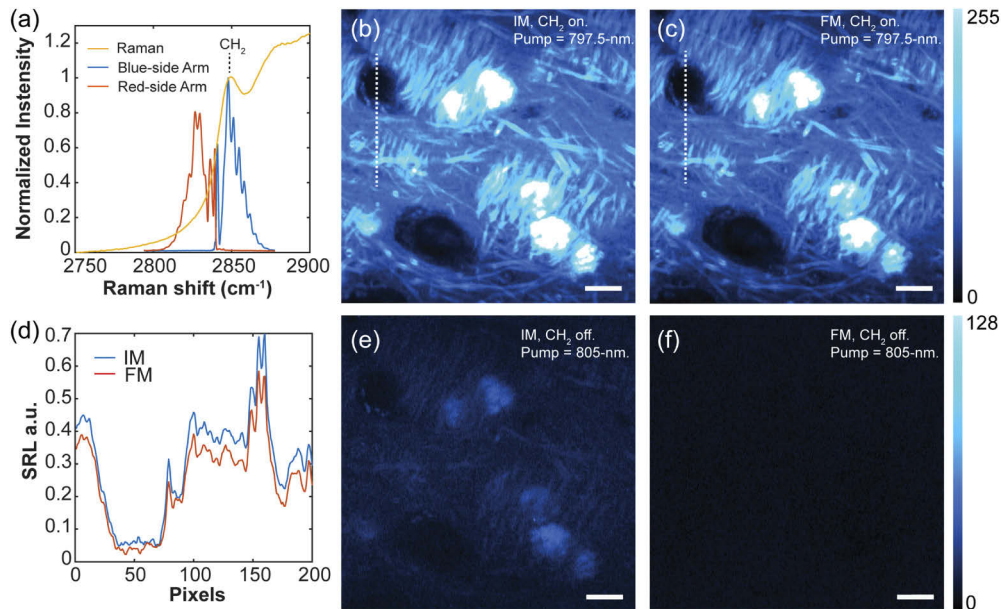
Fig. 4. FM-SRS imaging of lipid in mouse brain tissue. (a) The excitation configuration of CH_2 stretching mode. Blue curve for excitation energy blue-shifted arm (corresponding to red-shifted Stokes beam); red curve for excitation energy red-shifted arm (corresponding to blue-shifted Stokes beam); Yellow curve is the spontaneous Raman spectrum of brain tissue as a reference, the resonance peak of CH_2 stretching mode is indicated. (b) and (e) show the conventional IM-SRS imaging results of the on (pump at 797.5 nm) and off resonance (pump at 805-nm) channels, respectively. (c) and (f) show our FM-SRS imaging results of the on (pump at 797.5 nm) and off resonance (pump at 805 nm) channels, respectively. (d) shows the signal distributions on the dash lines in (b) (blue curve) and (c) (red curve), respectively. All imaging acquired with 20-mW pump beam and 30-mW Stokes beams. (b) and (c) share the same color bar, (e) and (f) share the same color bar. Scale bar: 10 μm.

2.4. Suppression of non-resonant cross-phase modulation background

We now demonstrate the background-free advantages of our FM-SRS. The cross-phase modulation, a ubiquitous non-resonant four-wave-mixing process, is well known to introduce substantial background for refractive-index-heterogeneous tissues and cells, hindering accurate quantitative studies in IM-based SRS microscopy [7,8,14,29]. We investigated both tissue samples and small vibrational-tag labeled cell samples (Fig. 4, 5).

The CH_2 stretching mode in brain tissue has a relatively broad linewidth (Fig. 4(a), shoulder on yellow curve). To perform FM-SRS imaging, ~15.6-nJ IR pulse energy was launched into the fiber, so that a strong spectral broadening could occur through SPM to achieve a 27-cm^{-1} frequency difference between the two Stokes arms (Fig. 4(a)). First, the red-shift arm (corresponding to Stokes blue shift arm, red curve in Fig. 4(a)) was blocked to perform standard IM-SRS as the control (Fig. 4(b), (e)). Later this arm was released to perform FM-SRS imaging (Fig. 4(c), (f)). As shown in Fig. 4(b) and (c), SRS imaging of the CH_2 stretching mode maps out the lipid distribution, which mainly concentrated in the myelin of axons. However, the lipid-rich axon bundles exhibit a refractive index significantly different from the surrounding tissues, resulting in large cross-phase background under IM detection (shown in the off-resonance channel (Fig. 4(e))). Importantly, when both Stokes beams are applied for FM-SRS, the broad cross-phase modulation background was effectively cancelled, as shown in the off-resonance FM-SRS channel (Fig. 4(f)).

Thanks to the proper frequency difference between two Stokes arms, the pure CH_2 signal is preserved to a large extent (Fig. 4(b)-(d)).

Vibrational tags often display narrow Raman linewidth (typically ~10-cm^{-1}) [6,30], which requires high spectral resolution. In our design, the bandwidths and frequency difference between the two Stokes arms can be controlled by the pulse energy launched into the fiber. This property enables an adaptive spectral resolution for Raman modes with different linewidths. As a demonstration, here we performed FM-SRS imaging of a polyyne marker LD2202 for lipid droplet tracking [24] (Fig. 5). To match with the narrow linewidth of ~12-cm^{-1} from the LD2202, a relatively low 6.2-nJ IR pulse was launched into the fiber to generate ~11-cm^{-1} frequency difference between the two Stokes arms (Fig. 5(a)). SRL spectrum of the LD2202 marker was recorded by FM-SRS with two peaks (one positive and one negative, corresponding to vibrational resonance with two Stokes beams modulated with a π-phase difference) separated by ~0.8-nm pump wavelength difference (~11-cm^{-1}) (Fig. 5(b)). Lipid droplets have relatively higher refractive index than other organelles inside cells, serving as the main source for cross-phase modulation background. This is illustrated by the IM-SRS image, in which the locations of lipid droplets show obvious cross-phase background in the off-resonance channel (Fig. 5(c), (d) and (g)). Again, the FM-SRS shows the advantages of successfully removing the background but preserving the pure vibrational signal from LD2202 marker (Fig. 5(e), (f) and (h)).

2.5. Suppression of electronic transition derived backgrounds

In addition to the non-resonant cross phase modulation, background interaction from electronic resonance can be much more intense and even overwhelm the relatively weak Raman signal. We next demonstrate our FM-SRS method can sufficiently suppress the overwhelming backgrounds originate from electronic transitions such as two-photon absorption and pump-probe interaction (i.e., hot luminescence [31,32]).

Melanin pigment is widely distributed in the skin of the popular black mouse model (C57BL/6J). The strong and broadband light absorption of melanin results in complex multiphoton processes, which introduces overwhelming background under the conventional IM-SRS excitation. Figure 6 shows the SRS imaging of label-free CH_2 stretching mode of wild type (C57BL/6J) mouse ear skin. Indeed, an overwhelming background is observed around the lipid-rich sebaceous gland under conventional IM-SRS imaging (Fig. 6(a), (c)), due to the presence of melanin residing in the melanocyte cells around the glands. Interestingly, this melanin-derived background almost totally vanished under our FM-SRS strategy, revealing relatively weak lipid signal of CH_2 mode near the sebaceous gland (Fig. 6(b), (d)). Hence our FM-SRS method can retrieve the relatively weak Raman signals from the overwhelming background originated from electronic transition.

Different from the above case where the target bond is separate from the background source, electronic-transition-related backgrounds can also arise from the target molecule itself [11], [12] (Fig. 7). Harnessing electronic resonance can enable up to 10^7 enhancement of the Raman cross sections for electronic coupled vibrational modes [12,33]. But as the pump energy approaches electronic resonance, the pump-probe background (i.e., hot luminescence) can increase faster than the SRS signal [34]. As shown previously [11], the pump should be detuned by more than two times of the homogeneous linewidth (Γ) of electronic transition to avoid significant background. Here we show that FM-SRS scheme could help to suppress this background and allow deeper electronic resonance. Figure 7(a) shows the absorption spectrum of our newly synthesized Raman dye. For the SRS excitation of its nitrile mode, the pump beam (yellow line, Fig. 7(a)) is very close to the rigorous electronic resonance, which would excite a large background in addition to the SRS signal. Indeed, the SRL spectrum of 1-mM DMSO solution recorded by IM-SRS confirms this result (blue curve, Fig. 7(b)).

The Raman dye used here displays relatively narrow linewidth for its nitrile mode (~10-cm^{-1}), which is designed for the purpose of performing super-multiplexed vibrational imaging [35]. As
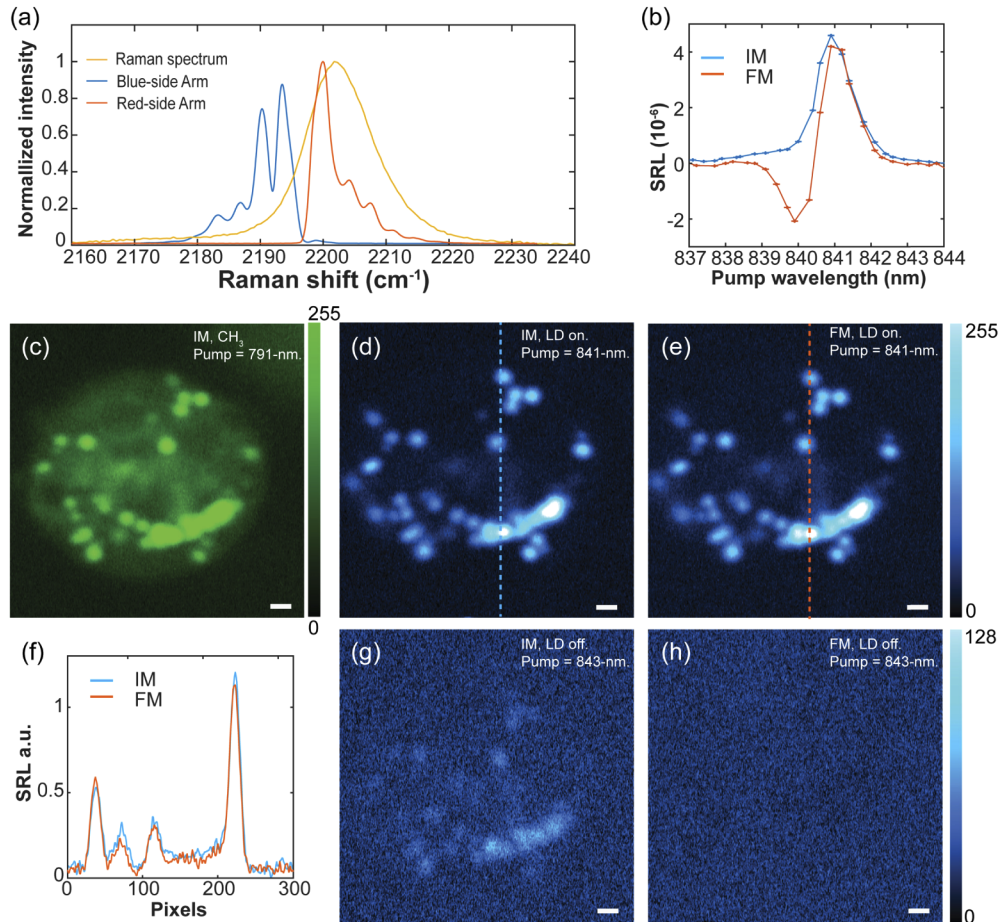
Fig. 5. FM-SRS imaging of polyyne-labeled lipid droplets in cells. (a) The excitation configuration for the lipid droplet marker. Blue curve for excitation energy blue-shifted arm (corresponding to red-shifted Stokes beam); red curve for excitation energy red-shifted arm (corresponding to blue-shifted Stokes beam); Yellow curve is the spontaneous Raman spectrum of the marker. (b) SRL spectra of the marker in 1-mM DMSO solution acquired by IM-SRS (blue curve) and our FM-SRS (red curve), respectively. (c) SRS imaging of the CH_3 stretching mode as a reference for the cell location. (d) and (g) show the conventional IM-SRS imaging results of the lipid droplet marker at its on (pump at 841-nm) and off resonance (pump at 843-nm) channels, respectively. (e) and (h) show our FM-SRS imaging results of the lipid droplet marker at its on (pump at 841 nm) and off resonance (pump at 843 nm) channels, respectively. (f) shows the signal distributions on the dash lines in (d) (blue curve) and (e) (red curve), respectively. All imaging acquired with 20-mW pump beam and 15-mW Stokes beams. (d) and (e) share the same color bar, (g) and (h) share the same color bar. Scale bar: 1 μm.
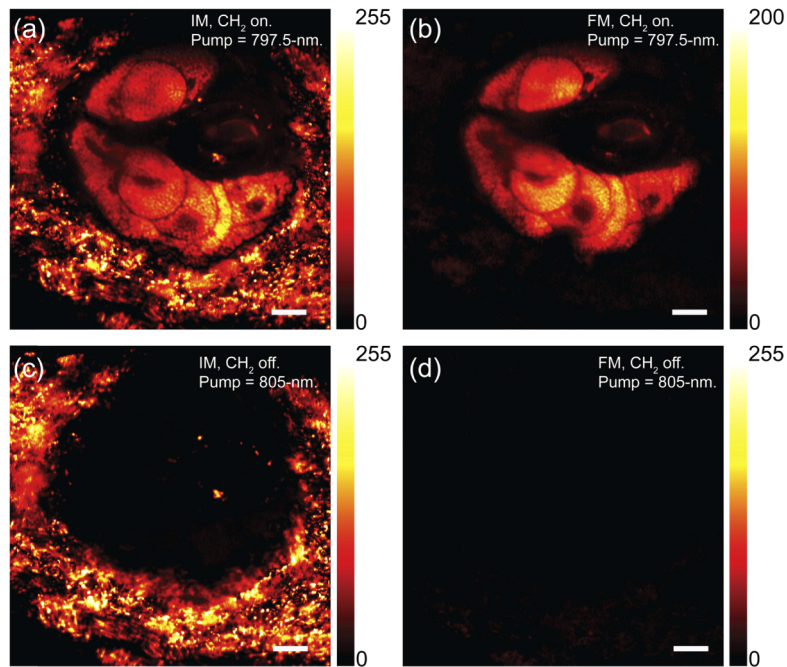
Fig. 6. FM-SRS imaging of sebaceous gland in wild type (C57BL/6J) mouse skin. (a) and (c) show the conventional IM-SRS imaging results of the CH_2 mode at its on resonance (pump at 797.5 nm) and off resonance (pump at 805 nm) channels, respectively. (b) and (d) show our FM-SRS imaging results of the CH_2 mode at its on (pump at 797.5 nm) and off resonance (pump at 805 nm) channels, respectively. All imaging acquired with 14-mW pump beam and 30-mW Stokes beams. Scale bar: 10 µm.

in the case of polyynes tag for lipid droplet tracking above (Fig. 5), the pulse power coupled into the fiber was set to 6.2-nJ to achieve the optimal spectral resolution. When we transfer to the FM-SRS mode, the background is totally cancelled, and only two resonance peaks (one positive and one negative) are observed, corresponding to the pure SRL signal of the nitrile mode (red curve, Fig. 7(b)). To further confirm the background can be efficiently removed in cell imaging, HeLa cells are labeled by conjugating the amine groups in cells with the NHS-ester linker of the dye (Fig. 7(c)-(g)). As anticipated, while strong background is observed in the off-resonance channels of IM-SRS imaging (Fig. 7(c), (e)), background nearly vanishes in off-resonance channels of FM-SRS imaging (Fig. 7(f), (h)), leaving the on-resonance FM-SRS channel with pure SRL signal (Fig. 7(g)). It is important to note that, to achieve successful canceling of the electronic-transition-related backgrounds, the energy difference between the two Stokes beams should be much smaller than the absorption linewidth of the chromophores so that they do not contribute to different multiphoton excitation. Because of this mechanism, some previous techniques with large energy difference between two Stokes beams [9,16] may not work well in this case.
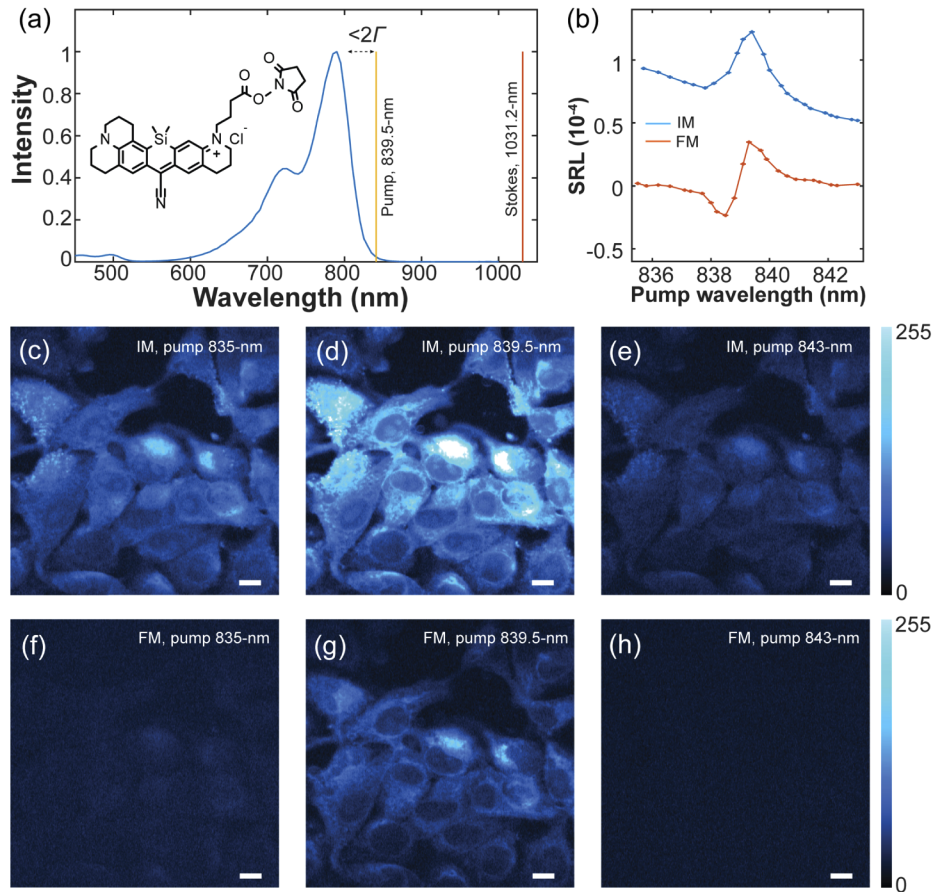
Fig. 7. FM-SRS imaging of cells labeled by Raman dye under close electronic resonance. (a) the absorption spectrum (blue curve) of our newly synthesized dye. The laser lines for the nitrile mode on-resonance excitation are provided, with red line for Stokes beam and yellow line for pump beam. (b) SRL spectra of 1-mM the dye molecule in DMSO solution acquired by IM-SRS (blue curve) and FM-SRS (red curve). (c), (d) and (e) show the conventional IM-SRS imaging results of the dye labeled cell at the blue-side off (pump at 835 nm), on (pump at 839.5 nm) and red-side off resonance (pump at 843 nm) channels of the nitrile mode, respectively. (f), (g) and (h) show our FM-SRS imaging results of the dye labeled cell at the blue-side off (pump at 835 nm), on (pump at 839.5 nm) and red-side off resonance (pump at 843 nm) channels of nitrile mode, respectively. All imaging acquired with 12-mW pump beam and 15-mW Stokes beams, and share the same color bar. Scale bar: 10 μm.

3. Conclusion

To summarize, we have developed a simple and robust FM-SRS microscopy by harnessing the spectral splitting effect of picosecond pulse propagation in the standard single-mode silica fiber (i.e., the original peak will evolve into new frequency lobes under proper nonlinear phase shift accumulated via SPM). This system is able to perform background-free narrowband SRS imaging based on a popular commercial picosecond laser system from APE Inc. (which is also used as the light source in the commercial integrated SRS microscope from Leica) with regular optics and conventional alignments (Fig. 3). In particular, the equal distribution of converted photons by SPM into the two Stokes bands naturally synchronizes their temporal fluctuations, resulting in superb signal stability and noise property (Fig. 3). Moreover, it allows an adaptive spectra resolution to achieve the optimal imaging performance for Raman modes with different linewidths. As we have demonstrated for various applications, the separation between the energy centers of the two Stokes arms can be tuned to ~11 cm^{-1} and 27 cm^{-1} when the pulse power coupled into the fiber (0.2 m) is set to 6.2 nJ and 15.6 nJ, respectively. Different fiber lengths would further tune the spectral splitting. Compared with the hyperspectral SRS approaches that record images across a series of excitation wavelengths for subsequent spectral analysis [36–38], this method performs single shot imaging of a target chemical bond without acquiring other channels for signal abstraction and unmixing. Therefore, if narrowband information is sufficient for the application, better temporal resolution can be anticipated for FM-SRS together with the ease of image registration and interpretation.

To showcase the generality, we achieved successful suppressing of backgrounds on various origins including the non-resonant cross-phase modulation (Fig. 4, 5) and the overwhelming electronic-transition-related backgrounds (Fig. 6, 7). Among the samples, both tissue samples (Fig. 4, 6) and cultured cells (Fig. 5, 7) have been demonstrated on a wide variety of imaging targets: label-free biomolecules (Fig. 4, 6), exogenous small molecule markers (Fig. 5) and Raman-active organic dyes (Fig. 7). In particular, successful suppressing of the overwhelming hot luminescent background in electronic resonance SRS imaging is shown for the first time (Fig. 7). This capability paves the way for the investigation of SRS imaging with rigorous electronic resonance, which would be more sensitive than the pre-resonance cases [11,12]. Besides SRS imaging, our FM strategy may find applications in other vibrational spectroscopy and microscopy, such as the recently developed stimulated Raman excited fluorescence (SREF) which also carries a certain broadband fluorescence background [39,40].

Appendix A: the simulation of pulse propagation in silica fiber

The simulation of picosecond pulse propagation in single-mode silica fiber is achieved by numerically solving the famous nonlinear Schrodinger equation (NSN) as shown below. The derivation and the basic principle can be found in the first four chapters of Agrawal's famous book [25].

$$i\frac{\partial U}{\partial \xi} = sgn(\beta_2)\frac{1}{2}\frac{\partial^2 U}{\partial \tau^2} - N^2|U|^2 U \qquad (1)$$

Here, $U(\xi, \tau)$ is the normalized complex field magnitude of the pulse (FWHM pulse duration T_0=2 ps), the solution of $U(\xi, \tau)$ contain all the temporal and spectral information of the pulse; $\xi = \frac{z}{L_D}$ is the distance normalized to dispersion length $\left(L_D = \frac{T_0^2}{\beta_2}\right)$, and $\beta_2 = -\frac{D\lambda^2}{2\pi c}$ is the group velocity dispersion in the fiber, D = -47.58 ps·nm^{-1}·km^{-1} at 1031.2-nm given by the fiber vendor, c is the light speed in vacuum; $\tau = \frac{t-z/v_g}{T_0}$ is the normalized time measured in the frame moving with the pulse with the group velocity v_g; sgn function gives the sign of the input value; $N^2 = \frac{\gamma P_0 T_0^2}{|\beta_2|}$, P_0 is the peak power of the pulse, $\gamma = \frac{\omega_0 n_2}{cA_{eff}}$ is the nonlinear parameter, ω_0 is the center frequency of the pulse, A_{eff} is the effective mode area, estimated by πw^2, and $w \approx 3\mu m$ is

half of the mode field diameter provided by the vendor, $n_2 \approx 3 \times 10^{-20}$ m²/W, is the nonlinear Kerr parameter for silica estimated at 1031.2-nm.

The initial normalized field amplitude of non-chirped sech² pulse is defined as,

$$U(0, \tau) = \mathrm{sech}(1.76\tau) \tag{2}$$

With the above configuration, Eq. (1) is solved numerically by standard partial differential equation solver in MATLAB. Then, the output temporal profile of the pulse is achieved by calculating $|U|^2$; spectral profile is achieved by calculating $|FT(U)|^2$, *FT* for Fourier transform. The results for 6.25-nJ pulse propagating in 1-m long single mode silica fiber (PM980-XP, Nufern) is shown in Fig. 8. Interestingly, the temporal profile does not change too much along the 1-m fiber, while the spectrum is continuously broadened, which makes SPM as an ideal mechanism of laser spectral broadening for FM-SRS application. Note that at 0.2-nm, the frequency component at the center band totally depleted, and two frequency lobes, one is red-shifted, the other blue-shifted, are generated (Fig. 8(b)). We used these two lobes as Stokes for FM-SRS imaging of Raman mode with narrow linewidth ($\sim$10-cm^{-1}) (Fig. 5, 7). Other useful position is $z = 0.5$-m and 0.9-m, these can be used for FM-SRS imaging of Raman modes with much wider linewidths. The small lobes near the center frequency is not a problem, because they will not affect the temporal profile (Fig. 8(a)), and wide Raman linewidth is not sensitive to those ripples on laser spectrum. It is very important to note that, to achieve those specific spectra, there is no need to change fibers with different lengths in real experiment. There is more convenient way, which is to change the input pulse energy. If the product of fiber length and pulse energy is the same, the output spectra will be the same (Fig. 8(b) and Fig. 2(b)), which means to achieve the same spectrum at position $z = 0.5$-m, we can keep the fiber length as 0.2-m but increase the input pulse energy to 15.6-nJ, which is what we did in the FM-SRS imaging for Raman modes with broad line shapes (see Fig. 4, 6).
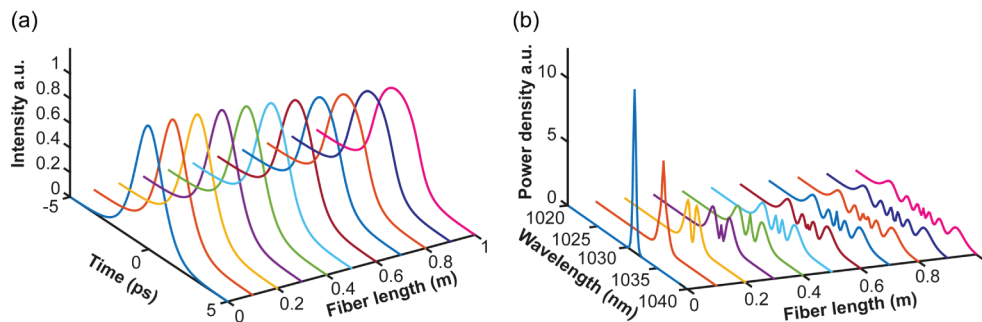

Fig. 8. The simulation results of temporal (a) and spectral (b) profiles of 6.25-nJ non-chirped 2-ps sech² pulses centered at 1031.2-nm as a function of propagation distance in single-mode silica fiber. all curves are normalized to the same pulse power.

Appendix B: The details of system construction

Fiber coupling: An aspheric lens (A397-B, Thorlabs) and the standard single-mode fiber launch system (MBT621D, Thorlabs) were used to coupling the IR beam into the 0.2-m long polarization maintained single-mode fiber (PM980-XP, Nufern). Before coupling, the laser beam diameter is adjusted by a telescope to fit the N.A. of the fiber. A coupling efficiency of $\sim$80% is easily achieved without too much alignment efforts.

Microscope construction: the home-build laser scanning microscope is based on an Olympus IX71 microscope. laser scanning was achieved by standard alignment of a 2D-galvanometer

(GVSM002, Thorlabs), a scan lens (Thorlabs, SL50-CLS2) and tube lens (Thorlabs, TL200-CLS2). A 60X water immersion objective (UPLSAPO, 1.2 N.A., Olympus) was used for all measurements. All imaging scanning and data acquisition were achieved by a NI card (PCI-6259, NI), and controlled by home-written LabVIEW programs. The whole optical alignment is sealed in a box. Otherwise, the airflow will introduce jitters of the time delay, resulting in detectable fluctuation on the FM-SRS signals.

Signal detection: The laser itself provide a 20-MHz modulation signal, it was amplified by a power amplifier (Mini-Circuits, ZHL-1-2W+) before sent to the modulator to achieve a modulation depth more than 90%. The forward-going pump and Stokes beams after samples were collected by a high NA IR-coated oil condenser (1.4 NA, Olympus), which is aligned by Köhler illumination. A high-speed large-area silicon PIN photodiode (S3590-09, Hamamatsu) was used as a detector. A high OD bandpass filter (ET890/220 m, Chroma) was placed in front of the photodiode to block the Stokes beam completely and transmit the pump beam. The photodiode was reversed biased by 64 V from a DC power supply to increase both the saturation threshold and response bandwidth. Signal output of the photodiode was then sent to a fast look-in amplifier (HF2LI, Zurich Instruments) for signal demodulation. The demodulated signal was digitalized by the NI card (PCI-6259, NI) driven by our home-written LabVIEW program. For laser fluctuation monitoring shown in Fig. 3(c), two photodiodes (DET10A2, Thorlabs) were used to simultaneous record the laser intensity, and a AC coupled dual-channel current amplifier (HF2TA, Zurich Instruments) with bandwidth limited by two lowpass filters (BLP-1.9+, Mini-Circuits) was used to read out the small fluctuations (less than 2%). The data was simultaneously collected by an oscilloscope (MDO3102, Tektronix).

Funding

Disclosures

The authors declare no conflicts of interest.

References

1. J.-X. Cheng and X. S. Xie, "Vibrational spectroscopic imaging of living systems: An emerging platform for biology and medicine," Science **350**(6264), aaa8870 (2015).
2. R. C. Prince, R. R. Frontiera, and E. O. Potma, "Stimulated Raman scattering: from bulk to nano," Chem. Rev. **117**(7), 5070–5094 (2017).
3. C. H. Camp Jr and M. T. Cicerone, "Chemically sensitive bioimaging with coherent Raman scattering," Nat. Photonics **9**(5), 295–305 (2015).
4. L. Wei, F. Hu, Z. Chen, Y. Shen, L. Zhang, and W. Min, "Live-cell bioorthogonal chemical imaging: stimulated Raman scattering microscopy of vibrational probes," Acc. Chem. Res. **49**(8), 1494–1502 (2016).
5. Q. Cheng, L. Wei, Z. Liu, N. Ni, Z. Sang, B. Zhu, W. Xu, M. Chen, Y. Miao, and L.-Q. Chen, "Operando and three-dimensional visualization of anion depletion and lithium growth by stimulated Raman scattering microscopy," Nat. Commun. **9**(1), 2942 (2018).
6. Y. Shen, F. Hu, and W. Min, "Raman Imaging of Small Biomolecules," Annu. Rev. Biophys. **48**(1), 347–369 (2019).
7. C. W. Freudiger, W. Min, B. G. Saar, S. Lu, G. R. Holtom, C. He, J. C. Tsai, J. X. Kang, and X. S. Xie, "Label-free biomedical imaging with high sensitivity by stimulated Raman scattering microscopy," Science **322**(5909), 1857–1861 (2008).
8. W. Min, C. W. Freudiger, S. Lu, and X. S. Xie, "Coherent nonlinear optical imaging: beyond fluorescence microscopy," Annu. Rev. Phys. Chem. **62**(1), 507–530 (2011).
9. P. Berto, E. R. Andresen, and H. Rigneault, "Background-free stimulated Raman spectroscopy and microscopy," Phys. Rev. Lett. **112**(5), 053905 (2014).
10. D. Fu, W. Yang, and X. S. Xie, "Label-free imaging of neurotransmitter acetylcholine at neuromuscular junctions with stimulated Raman scattering," J. Am. Chem. Soc. **139**(2), 583–586 (2017).
11. L. Wei, Z. Chen, L. Shi, R. Long, A. V. Anzalone, L. Zhang, F. Hu, R. Yuste, V. W. Cornish, and W. Min, "Super-multiplex vibrational imaging," Nature **544**(7651), 465–470 (2017).

12. L. Shi, H. Xiong, Y. Shen, R. Long, L. Wei, and W. Min, "Electronic resonant stimulated raman scattering micro-spectroscopy," J. Phys. Chem. B **122**(39), 9218–9224 (2018).

13. D. Zhang, M. N. Slipchenko, D. E. Leaird, A. M. Weiner, and J.-X. Cheng, "Spectrally modulated stimulated Raman scattering imaging with an angle-to-wavelength pulse shaper," Opt. Express **21**(11), 13864–13874 (2013).

14. K. Popov, A. Pegoraro, A. Stolow, and L. Ramunno, "Image formation in CARS and SRS: effect of an inhomogeneous nonresonant background medium," Opt. Lett. **37**(4), 473–475 (2012).

15. B. Levine and C. Bethea, "Frequency-modulated shot noise limited stimulated Raman gain spectroscopy," Appl. Phys. Lett. **36**(4), 245–247 (1980).

16. B. G. Saar, G. R. Holtom, C. W. Freudiger, C. Ackermann, W. Hill, and X. S. Xie, "Intracavity wavelength modulation of an optical parametric oscillator for coherent Raman microscopy," Opt. Express **17**(15), 12532–12539 (2009).

17. F. Ganikhanov, C. L. Evans, B. G. Saar, and X. S. Xie, "High-sensitivity vibrational imaging with frequency modulation coherent anti-Stokes Raman scattering (FM CARS) microscopy," Opt. Lett. **31**(12), 1872–1874 (2006).

18. B. Sarri, R. Canonge, X. Audier, E. Simon, J. Wojak, F. Caillol, C. Cador, D. Marguet, F. Poizat, and M. Giovannini, "Fast stimulated Raman imaging for intraoperative gastro-intestinal cancer detection," *arXiv preprint arXiv:1902.08859* (2019).

19. W. Yang, A. Li, Y. Suo, F.-K. Lu, and X. S. Xie, "Simultaneous two-color stimulated Raman scattering microscopy by adding a fiber amplifier to a 2 ps OPO-based SRS microscope," Opt. Lett. **42**(3), 523–526 (2017).

20. B.-C. Chen, J. Sung, and S.-H. Lim, "Chemical imaging with frequency modulation coherent anti-Stokes Raman scattering microscopy at the vibrational fingerprint region," J. Phys. Chem. B **114**(50), 16871–16880 (2010).

21. A. H. Hill, E. Munger, A. T. Francis, B. Manifold, and D. Fu, "Frequency Modulation Stimulated Raman Scattering Microscopy through Polarization Encoding," J. Phys. Chem. B **123**(40), 8397–8404 (2019).

22. H. Yamakoshi, K. Dodo, A. Palonpon, J. Ando, K. Fujita, S. Kawata, and M. Sodeoka, "Alkyne-tag Raman imaging for visualization of mobile small molecules in live cells," J. Am. Chem. Soc. **134**(51), 20681–20689 (2012).

23. L. Wei, F. Hu, Y. Shen, Z. Chen, Y. Yu, C.-C. Lin, M. C. Wang, and W. Min, "Live-cell imaging of alkyne-tagged small biomolecules by stimulated Raman scattering," Nat. Methods **11**(4), 410–412 (2014).

24. F. Hu, C. Zeng, R. Long, Y. Miao, L. Wei, Q. Xu, and W. Min, "Supermultiplexed optical imaging and barcoding with engineered polyynes," Nat. Methods **15**(3), 194–200 (2018).

25. G. P. Agrawal, *Nonlinear fiber optics* (Springer, 2013).

26. R. Stolen and C. Lin, "Self-phase-modulation in silica optical fibers," Phys. Rev. A **17**(4), 1448–1453 (1978).

27. J. M. Dudley and J. R. Taylor, *Supercontinuum generation in optical fibers* (Cambridge University Press, 2010).

28. W. Tomlinson, R. Stolen, and C. Shank, "Compression of optical pulses chirped by self-phase modulation in fibers," J. Opt. Soc. Am. B **1**(2), 139–149 (1984).

29. L. Shi, C. Zheng, Y. Shen, Z. Chen, E. S. Silveira, L. Zhang, M. Wei, C. Liu, C. de Sena-Tomas, and K. Targoff, "Optical imaging of metabolic dynamics in animals," Nat. Commun. **9**(1), 2995 (2018).

30. Z. Zhao, Y. Shen, F. Hu, and W. Min, "Applications of vibrational tags in biological imaging by Raman microscopy," Analyst **142**(21), 4018–4029 (2017).

31. Y. Shen, "Distinction between resonance Raman scattering and hot luminescence," Phys. Rev. B **9**(2), 622–626 (1974).

32. R. R. Frontiera, S. Shim, and R. A. Mathies, "Origin of negative and dispersive features in anti-Stokes and resonance femtosecond stimulated Raman spectroscopy," J. Chem. Phys. **129**(6), 064507 (2008).

33. S. Shim, C. M. Stuart, and R. A. Mathies, "Resonance Raman Cross-Sections and Vibronic Analysis of Rhodamine 6G from Broadband Stimulated Raman Spectroscopy," ChemPhysChem **9**(5), 697–699 (2008).

34. L. Wei and W. Min, "Electronic Pre-resonance Stimulated Raman Scattering Microscopy," J. Phys. Chem. Lett. **9**(15), 4294–4301 (2018).

35. Y. Miao, L. Shi, F. Hu, and W. Min, "Probe design for super-multiplexed vibrational imaging," Phys. Biol. **16**(4), 041003 (2019).

36. Y. Ozeki, W. Umemura, Y. Otsuka, S. Satoh, H. Hashimoto, K. Sumimura, N. Nishizawa, K. Fukui, and K. Itoh, "High-speed molecular spectral imaging of tissue with stimulated Raman scattering," Nat. Photonics **6**(12), 845–851 (2012).

37. D. Fu, G. Holtom, C. Freudiger, X. Zhang, and X. S. Xie, "Hyperspectral Imaging with Stimulated Raman Scattering by Chirped Femtosecond Lasers," J. Phys. Chem. B **117**(16), 4634–4640 (2013).

38. C.-S. Liao, K.-C. Huang, W. Hong, A. J. Chen, C. Karanja, P. Wang, G. Eakins, and J.-X. Cheng, "Stimulated Raman spectroscopic imaging by microsecond delay-line tuning," Optica **3**(12), 1377–1380 (2016).

39. H. Xiong, L. Shi, L. Wei, Y. Shen, R. Long, Z. Zhao, and W. Min, "Stimulated Raman excited fluorescence spectroscopy and imaging," Nat. Photonics **13**(6), 412–417 (2019).

40. H. Xiong, N. Qian, Y. Miao, Z. Zhao, and W. Min, "Stimulated Raman Excited Fluorescence Spectroscopy of Visible Dyes," J. Phys. Chem. Lett. **10**(13), 3563–3570 (2019).